ROSAT X-RAY OBSERVATIONS OF THE RADIO GALAXY NGC 1316 (FORNAX A)

D.-W. KIM

Chungnam National University, Taejon, 305-764, South Korea, and Harvard-Smithsonian Center for Astrophysics,
60 Garden Street, Cambridge, MA 02138

AND

G. FABBIANO AND G. MACKIE[1]

Harvard-Smithsonian Center for Astrophysics, 60 Garden Street, Cambridge, MA 02138

ABSTRACT

We have observed NGC 1316 (Fornax A) with the *ROSAT* HRI. In this paper, we present the results of these observations and complement them with the spectral analysis of the archival PSPC data. The spectral properties suggest the presence of a significant component of thermal X-ray emission (greater than 60%), amounting to $\sim 10^9 \, M_\odot$ of hot interstellar matter (ISM). Within 3′ from the nucleus of NGC 1316, the HRI X-ray surface brightness falls as r^{-2}. In the inner $\sim 40″$, the X-ray surface brightness is significantly elongated ($\epsilon \sim 0.3$). This flattened X-ray feature is confirmed by a straightforward statistics test as well as moment analysis. By comparing the morphology of the X-ray emission with the distribution of optical dust patches, we find that the X-ray emission is significantly reduced at the locations where the dust patches are more pronounced, indicating that at least some of the X-ray photons are absorbed by the cold ISM. We also compare the distribution of the hot and cold ISM with that of the ionized gas, using recently obtained $H\alpha$ CCD data. We find that the ionized gas is distributed roughly along the dust patches and follows the large-scale X-ray distribution at $r > 1′$ from the nucleus. However, there is no one-to-one correspondence between ionized gas and hot gas. Both morphological relations and kinematics suggest different origins for hot and cold ISM. The radio jets in projection appear to pass perpendicularly through the central X-ray ellipsoid. Comparison of thermal and radio pressures suggests that the radio jets are confined by the surrounding hot gaseous medium.

Subject headings: galaxies: individual (NGC 1316) — galaxies: ISM — galaxies: jets — X-rays: galaxies

1. INTRODUCTION

NGC 1316 (Fornax A, Arp 154) is a giant elliptical galaxy in the poor Fornax cluster. This galaxy exhibits many unusual features for an elliptical galaxy, including pronounced dust patches, $H\alpha$ filaments, ripples, and loops (see, e.g., Arp 1966; Schweizer 1980; Carter et al. 1983; Mackie & Fabbiano 1998). The distribution of the optical surface brightness reveals an extensive envelope, making NGC 1316 a typical D (or cD) galaxy (Schweizer 1980). It has one of the most pronounced shell systems observed in early-type galaxies (Malin & Carter 1983). These features all point to a recent merging in NGC 1316 (see, e.g., Schweizer 1980).

In the radio (0.03–5 GHz), Fornax A is one of the brightest objects in the sky ($L = 2 \times 10^{42}$ ergs s^{-1}; Ekers et al. 1983). It contains giant radio lobes (Wade 1961), separated by $\sim 30′$ (~ 240 kpc), consisting of polarized, organized filaments (Fomalont et al. 1989). A faint bridge between the lobes is displaced to the south of the galaxy center and S-shaped and nuclear radio jets are present, implying a significantly violent action in the galaxy history, as also suggested by the optical data (see, e.g., Ekers et al. 1983; Geldzahler & Fomalont 1984). The nucleus of NGC 1316 hosts a low-luminosity AGN: optically it has a LINER-type spectrum (Véron-Cetti & Véron 1986; Baum, Heckman, & van Breugel 1992), it contains a radio core (Geldzahler & Fomalont 1984) and *HST* observations have revealed a nuclear UV-bright point source (Fabbiano, Fassnacht, & Trinchieri 1994b). NGC 1316 also contains

complex, multiphase ISM: it has been detected in optical emission lines from ionized gas (see, e.g., Schweizer 1980; Phillips et al. 1986; Véron-Cetti & Véron 1986), *IRAS* far-infrared emission (Knapp et al. 1989), and CO lines of molecular gas (Wiklind & Henkel 1989; Sage & Galletta 1993).

In X-rays, NGC 1316 was detected with *Einstein* (Fabbiano, Kim, & Trinchieri 1992) and belongs to a group with the lowest L_X/L_B ratio among E and S0 galaxies (Kim, Fabbiano, & Trinchieri 1992b). Therefore, based on the global amount of X-ray emission, NGC 1316 does not necessarily contain a large amount of hot ISM (see Fabbiano, Gioia, & Trinchieri 1988). In this, it is similar to other galaxies which may have experienced recent mergers (Hibbard et al. 1994; Fabbiano & Schweizer 1995). *ROSAT* PSPC (Feigelson et al. 1995), and *ASCA* observations (Kaneda et al. 1995) have revealed the presence of extended inverse Compton X-ray emission at the locations of radio lobes.

In this paper, we discuss the results of a reanalysis of the archival *ROSAT* (Trumper 1983) PSPC observation of NGC 1316, and we report for the first time the results of high-resolution X-ray observation with the *ROSAT* HRI. The HRI has $\sim 5″$ resolution (David et al. 1993), comparable to that of ground-based radio and optical data. With these data we establish the presence of a hot ISM in NGC 1316 and correlate its properties to that of the other phases of the ISM. We also explore possible interactions between this hot ISM and the active radio nucleus.

This paper is structured as follows: in § 2, we present the results of the *ROSAT* HRI (§ 2.1 and § 2.2) and the *ROSAT* PSPC data analysis (§ 2.3); in § 3, we compare the X-ray

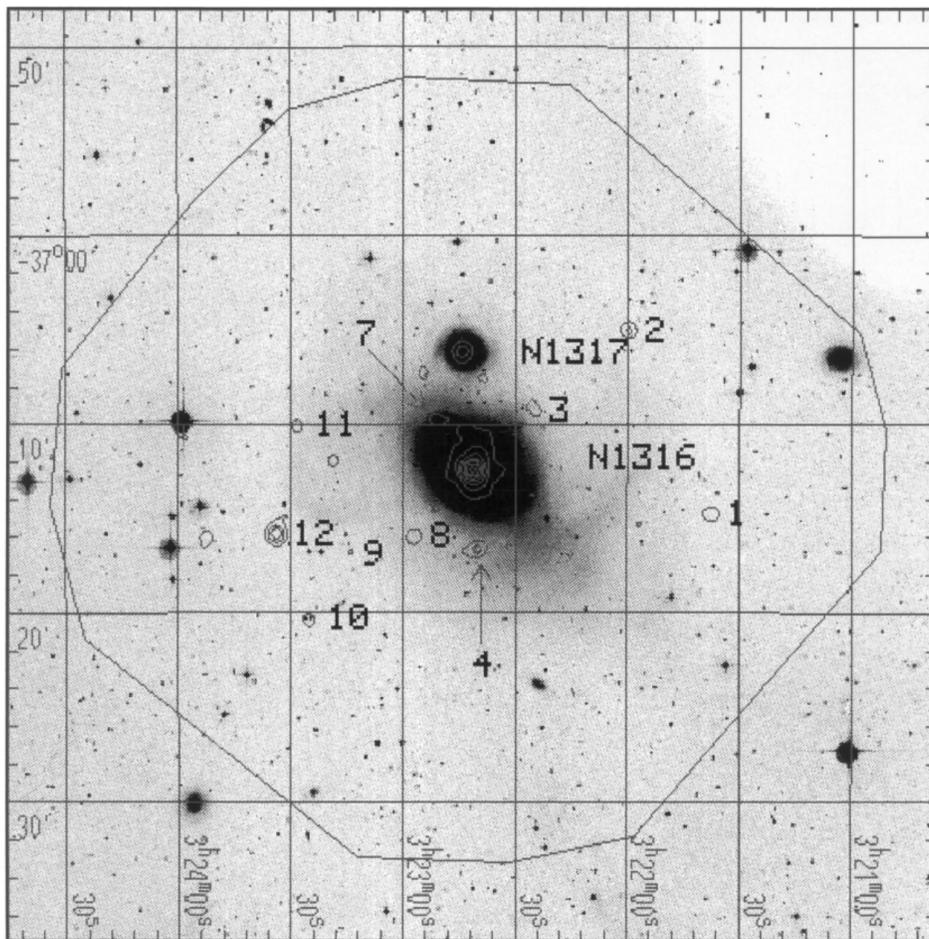[1] Visiting Astronomer, Cerro Tololo Inter-American Observatory.

FIG. 1.—Entire field of view of this HRI observation (NGC 1316 and NGC 1317). X-ray contours are overlaid on the optical image obtained from the Digital Sky Survey. X-ray image is binned with a pixel size of 8″, background-subtracted and smoothed with a Gaussian of $\sigma = 16″$. Octagonal shape indicates the boundary of the HRI detector. Source numbers are ordered by an increasing R.A. (see Table 2). R.A., and decl. are in J2000.

data with the optical and radio data; finally, in § 4 we discuss the implications of our results.

2. X-RAY OBSERVATIONS

NGC 1316 was observed with the *ROSAT* HRI on 1994 January 14 and 1994 July 7–10, for a total exposure time ~40 ks (three-fourths of total observations were obtained in the July run). The two data sets are consistent with each other within the observational uncertainty. We present the combined results except as mentioned in § 2.1. The field of view of this observation also includes the companion elliptical galaxy NGC 1317 (Fig. 1). The observational log and basic parameters of both galaxies are given in Table 1. NGC 1316 was also observed with the *ROSAT* PSPC (Feigelson et al. 1995), and we used the PSPC archival data to determine spectral parameters.

Given the limited statistics of our HRI observation, we have used various binning and smoothing factors to investigate both large-scale (a few arcminutes) and small-scale ($\lesssim 1'$) features. We used both IRAF and software we developed to analyze our data. We adopt a distance to NGC 1316 of 27.2 Mpc using $H_0 = 50$ km s^{-1} Mpc^{-1} (Fabbiano et al. 1992).

To extract source data, the field background must be subtracted. We found that estimates from the background map generated by the standard *ROSAT* SASS processing

and from local measures of the background in concentric annuli around the sources agree well with each other. We will present results obtained with the local background subtraction.

2.1. *X-Ray Emission Features and Sources*

The entire observed field of view is shown in Figure 1, where the X-ray contour map is overlaid on the optical image obtained from the Digitized Optical Survey.[2] The X-ray image was binned with a pixel size of 8″ and smoothed with a Gaussian of $\sigma = 16″$. The background is not subtracted. The octagonal shape indicates the boundary of the HRI detector. The figure shows a strong X-ray source at the center of the field, corresponding to the optical position of NGC 1316. Also X-ray emission is detected at the optical position of NGC 1317 (6″.3 to north of NGC 1316). In addition, 10 pointlike sources (above 3 σ) are detected in the observed field. The source position, radius of the count extraction circle, and X-ray count for each source are listed in order of R.A. in Table 2. The corresponding source numbers are marked in Figure 1. X-ray counts were

TABLE 1

BASIC PARAMETERS

Parameter	NGC 1316	NGC 1317
R.A. (J2000)[a]	3 22 41.6	3 22 44.7
Decl. (J2000)[a]	−37 12 28	−37 6 10
B_T° (mag)[a]	9.40	11.81
D (Mpc)[b]	27.2	27.2
D_{25} (arcsec)[a]	721	165
N_H (cm^{-2})[c]	2.0×10^{20}	2.0×10^{20}
HRI observed date[d]	1994 Jan 14	1994 Jan 14
HRI exp time (s)[d]	11038	11038
HRI observed date[e]	1994 Jul 7–10	1994 Jul 7–10
HRI exp time (s)[e]	29403	29403
PSPC observed date	1992 Jan 13–20	1992 Jan 13–20
PSPC exp time (s)	25500	25500
log F_X (IPC) ergs s^{-1} cm^{-2}[f]	2.0×10^{-12}	$<2.7 \times 10^{-13}$

[a] Right ascension (R.A.), declination (decl.), total face-on B magnitude (B_T°), and major isophotal diameter measured at $B = 25$ mag arcsec^{-2} (D_{25}) taken from de Vaucouleurs et al. 1991 (RC3).

[b] Distance from Fabbiano et al. 1992.

[c] Galactic line of sight H I column density from Starks et al. 1992.

[d] Sequence number 600255n00.

[e] Sequence number 600255a01.

[f] IPC flux from Fabbiano et al. 1992. Fluxes were estimated in a energy range of 0.2–4.0 keV for a Raymond-Smith model with solar abundance $kT = 1$ keV and line of sight N_H. The count extraction radi is $r = 450''$ for NGC 1316.

extracted from circular regions centered on their X-ray centroids. The radius was determined with the radial profile of the X-ray surface brightness (§ 2.2). Typically these radii extend to where the surface brightness is within ~3%–4% of the background. The background counts were extracted in annuli $r = 60''$–$200''$, except for NGC 1316 where an annulus $r = 200''$–$400''$ is used.

With the HRI observation of NGC 1316 we can trace the X-ray emission out to $170''$, or 22.4 kpc at an adopted distance of 27.2 Mpc (see § 2.2). However, the X-ray emission is extended at least to $1000''$ (Fabbiano et al. 1992; Feigelson et al. 1995). The other sources (including NGC 1317) are pointlike. Except for NGC 1316 and 1317, the sources are not identified with known objects in the SIMBAD catalog.

Source 2 and 12 are possibly variable. Their count rates from the two HRI observing epochs (Table 1) are significantly different (above 3 σ), while count rates of other

sources are consistent within the count errors between the two observations (see Table 3). The small numbers of source counts do not warrant further temporal analysis.

The number of serendipitous sources (omitting the target galaxy) found in this observation is consistent with the expected number of background sources. According to the log N–log S function (Hasinger et al. 1993), we would have about nine sources within a circular area of radius $15'$ and a limiting flux 1.8×10^{-14} ergs s^{-1} cm^{-2} in 0.5–2.0 keV, which corresponds to the faintest among detected sources (Table 2) for a power-law spectrum with $\alpha_E = 1$.

Figure 2 provides a close-up view of the NGC 1316 X-ray image, which was binned with a pixel size of $2''$ and smoothed with a Gaussian of $\sigma = 4''$, corresponding to FWHM = $11''.3$ for an on-axis point source. This image covers a $3' \times 3'$ field which falls inside the optical galaxy ($12' \times 8'.5$ in $D_{25} \times d_{25}$; see Table 1). Inside the central arc-

TABLE 2

X-RAY SOURCES

Source Number	X (pixels)	Y (pixels)	Radius[c] (arcsec)	Off-Axis (arcmin)	Vignetting Correction	Net (counts)	Error	F_X[e] (10^{-13})
1	5599.86	3823.70	30	12.9	1.076	67.44	15.77	0.53
2	5075.38	4998.42	25	10.9	1.055	89.45[d]	14.96	0.69
3	4468.47	4499.67	30	4.4	1.012	48.61	15.52	0.36
4	4104.82	3607.70	25	4.7	1.013	86.11	15.30	0.64
5[a]	4076.98	4108.50	170	...	...	2047.79	85.77	14.99
6[b]	4009.78	4862.26	20	6.2	1.020	120.29	15.05	0.90
7	3842.10	4436.98	25	3.4	1.008	35.52	13.19	0.26
8	3702.10	3687.70	30	5.1	1.015	68.92	16.08	0.51
9	3296.79	3583.91	15	8.1	1.033	31.89	9.79	0.24
10	3041.20	3157.04	25	12.0	1.065	53.90	13.76	0.42
11	2959.06	4396.66	20	9.7	1.045	44.42	11.83	0.34
12	2823.38	3703.22	20	11.2	1.057	201.14[d]	17.81	1.56

[a] NGC 1316.

[b] NGC 1317.

[c] Background counts were extracted in annuli ($r = 200''$–$400''$ for NGC 1316; $r = 60''$–$200''$ for all other sources).

[d] Variable (see Table 3).

[e] Fluxes were estimated in a energy range of 0.1–2.4 keV for a Raymond-Smith model with solar abundance, $kT = 1$ keV and line of sight N_H. Vignetting correction was applied.

SOURCE NUMBER	1994 JANUARY		1994 JULY		DIFFERENCE (σ)
	Rate	Error	Rate	Error	
2	−0.47	0.56	3.22	0.46	5.09
12	7.81	1.04	3.92	0.46	3.41

NOTE.—Rates and errors are in unit of counts in 1000 s.

minute, the X-ray emission is elongated along the northeast-southwest direction, following the optical major axis (P.A. = 50°; RC3), while in a larger scale (∼2′), the X-ray emission is extended along the north-south direction. This extension is more pronounced toward the north (see also Fig. 1).

The observed northeast-southwest elongation inside $r \sim 1'$ is intriguing if real because it may be related to a disk forming in the rotating cooling flow (§ 4.2) and because the radio jet in projection appears to propagate perpendicular to the direction of this elongation (§ 4.3). To determine its statistical significance, we first applied a straightforward test by comparing counts and errors in angular sectors at different position angles. We then applied more sophisticated tests: a Monte Carlo simulation and moment analysis. Figure 3 compares the counts at different position angles and gives the significance of differences. Overall the difference between counts extracted in the northeast-

southwest (P.A. = 30°–70°, 210°–250°) and northwest-southeast (P.A. = 120°–160°, 300°–340°) is very significant with a signal to noise ratio of 7.7 σ within $r < 40''$.

To estimate whether the flattening of the X-ray isophotes at small radii is due to chance positioning of a few noise "blobs" from an underlying spherical distribution, we have run a Monte Carlo simulation. This involves (1) choosing a spherical model, (2) creating a set of "observations" in which Poisson noise is added to the model and each X-ray is distributed taking into account the HRI PRF, and (3) then determining the chance probability of occurrence of the observed features. We generated a smooth model image by adopting the X-ray radial profile determined in § 2.2 under the assumption of spherical symmetry. Then we normalized the model image and added background counts to match with our HRI observation. We produced a set of 100 "observations" with a pixel size of 2″ (as in Fig. 2) by estimating Poisson deviate for each pixel value and distributing the photon according to the PRF. To estimate how often we obtain an elliptical surface brightness by chance, we examined simulated images after smoothing with the same Gaussian σ as in Figure 2. Out of 100 images, no ellipticity as significant as that of Figure 2 is seen. In our simulations, we also added serendipitous sources at random positions according to the log N–log S function (Hasinger et al. 1993) to verify whether a few undetected point sources can mimic our observed features. However, the results do not change appreciably. In conclusion, the chance probabil-
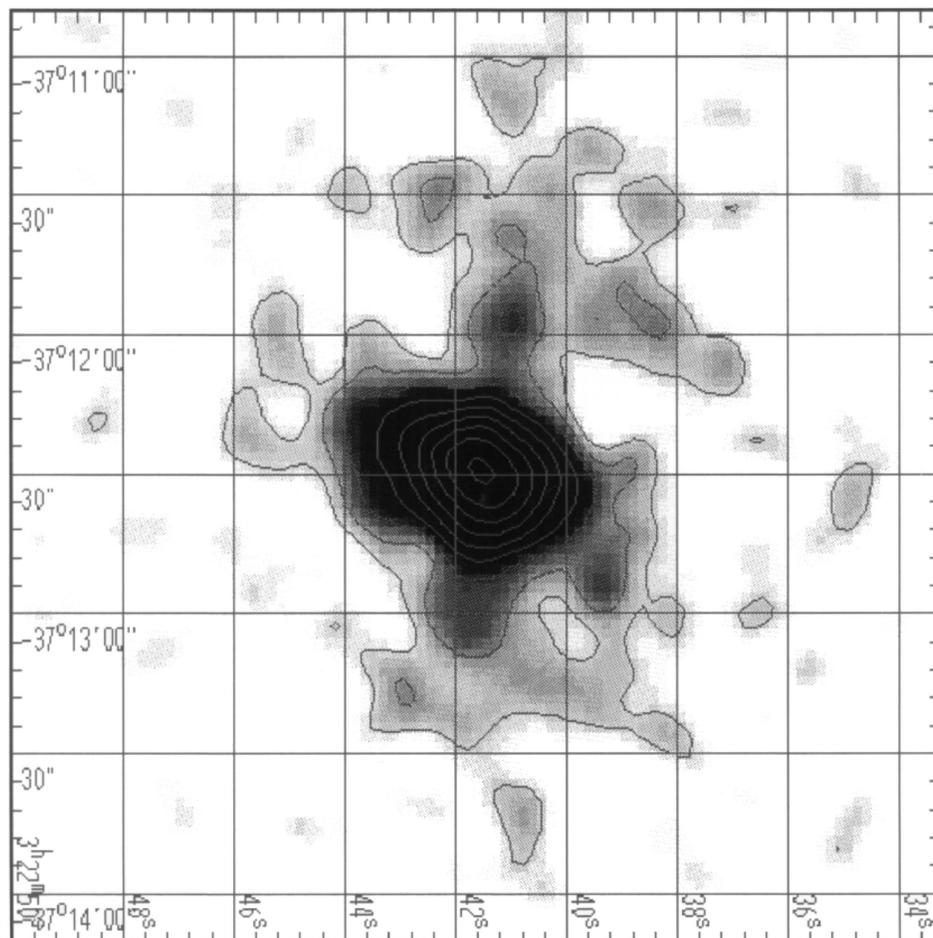

FIG. 2.—Close-up view of the X-ray image (with a pixel size of 2″ and a Gaussian σ of 4″). Contours indicate isophotes at 5%–95% of the peak with eight steps. R.A. and decl. are in J2000.
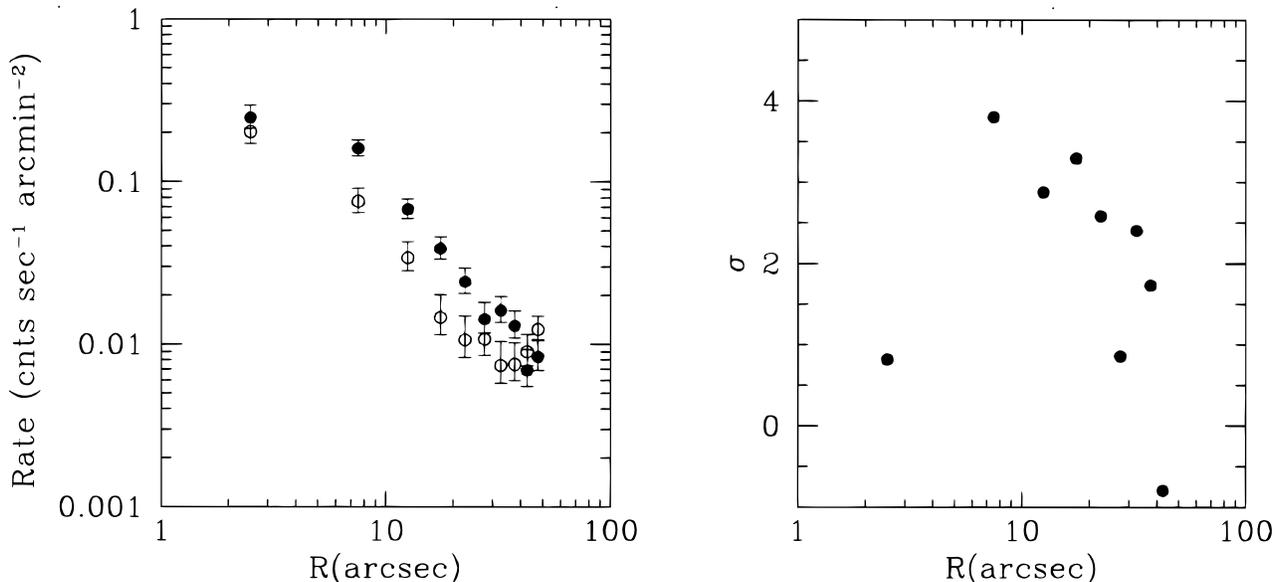
Fig. 3.—(*a*) Radial distribution of X-ray counts extracted in different angular sectors. Filled circles are for the northeast-southwest sector (P.A. = 30°–70°, 210°–250°), and open circles are for northwest-southeast (P.A. = 120°–160°, 300°–340°). (*b*) Significance of count differences between two angular sectors.

ity to generate the observed, elongated distribution of the inner X-ray surface brightness out of a circularly symmetrical distribution is less than 1%.

To parameterize the X-ray surface brightness distribution, we have applied a moment analysis (see fore details, Buote & Canizares 1994 and Carter & Metcalfe 1980). Ellipticities (ϵ) and position angles of the semimajor axis (θ) are iteratively determined by computing two-dimensional moments of inertia within elliptical apertures. We used an unsmoothed, raw image (2″ pixel) with background included. The measured ellipse parameters with a semimajor axis varying from 10″ to 50″ are $\epsilon = 0.28 \pm 0.05$ and $\theta = 56° \pm 8°$. We have also applied ellipse fitting (see, e.g., Jedrzejewski 1987), using the IRAF/STSDAS package to the smoothed image in Figure 2. The derived position angle and ellipticity are consistent with those determined by the moment analysis within their uncertainties.

Figure 4 shows the central region in greater detail with a pixel size of 1″ and smoothed with a Gaussian of $\sigma = 2″$ which corresponds to an on-axis beam of 6″.9 FWHM. In this scale the core surface brightness divides into double peaks, separated by 7″.3. The optical center (RC3) is close (within arcseconds) to the X-ray centroid determined with the image in Figure 2 and falls in the middle of the double peaks shown in Figure 4. Also noticeable are larger scale valleys at P.A. $\simeq 120°$ and P.A. $\simeq 320°$ which apparently bisect the core if extended to the center.

The double peaks and the southeast-northwest X-ray valleys are not caused by telescope aspect problems. We used only data obtained in the July run (see Table 1) to avoid a possible mismatch of the galaxy centers in the two observations due to aspect uncertainties, although source positions differ by less than 2″. The data obtained in the January run also present the same features but with larger statistical noise. To further check potential aspect problems, we applied the same binning and smoothing to pointlike sources within the observed field. Sources 4, 7, and 8, which are within 5′ from the field center (therefore the HRI PRF is similar to the on-axis one; David et al. 1993), are all circularly shaped, while sources 2 and 12, both at 11′ off-axis

distance (the PRF may not be circular), exhibit randomly elongated distribution.

The observed features are very interesting because the radio jet (Geldzahaler & Fomalont 1984) in projection appears to pass through the X-ray valleys (§ 3). However, the relatively low X-ray counts obtained in this high-resolution image may produce an artificial feature by chance positioning of a few noise "blobs." To explore this possibility, we have rerun a Monte Carlo simulation as described above. Out of 100 simulations with a resolution same as Figure 4 (1″ pixel and $\sigma = 2″$), three images exhibit double peaks and valleys, although not as significant as the observed. These simulation results imply that the existence of the double peaks and the X-ray valleys, although suggestive, is not conclusive and requires confirmation by deeper observation.

2.2. *Radial Profile*

Figure 5 shows the radial profile of the X-ray surface brightness measured in concentric rings centered on the NGC 1316 X-ray centroid (Table 2). The raw, background, and net counts are indicated by open squares, a solid line, and filled squares, respectively. The emission is extended out to 170″, 22 kpc at the adopted distance of 27.2 Mpc. To this profile, we fitted a King approximation model, $\Sigma_X \sim [1 + (r/a)^2]^{-3\beta + 0.5}$, convolved with the HRI point response function. (In the case of gaseous emission, β is related to a true isothermal value by $\beta_i = 1.5 \times \beta$; e.g., Sarazin 1988). Best-fit model, fit residuals, and confidence contours are shown in Figure 6. The best-fit parameters and 90% confidence range with two interesting parameters (in parenthesis) are core radius $a = 4″.1$ (3″.1–5″.0) and slope $\beta = 0.51$ (0.49–0.54), yielding $\chi^2 = 14.8$ for 9 degrees of freedom. The estimated slope corresponds to $\Sigma_X \sim r^{-2.06(1.94-2.24)}$ for $r \gg a$. This is close to that of the optical brightness distribution. Using the data in Schweizer (1981), we estimated the slope of the V_4 (5300–6400 Å) surface brightnesses in $r = 30″$ to 300″ to be 2.02 ± 0.06. The radial slope measured with the red continuum image (§ 3) does not differ significantly. We also used the PSPC data to derive
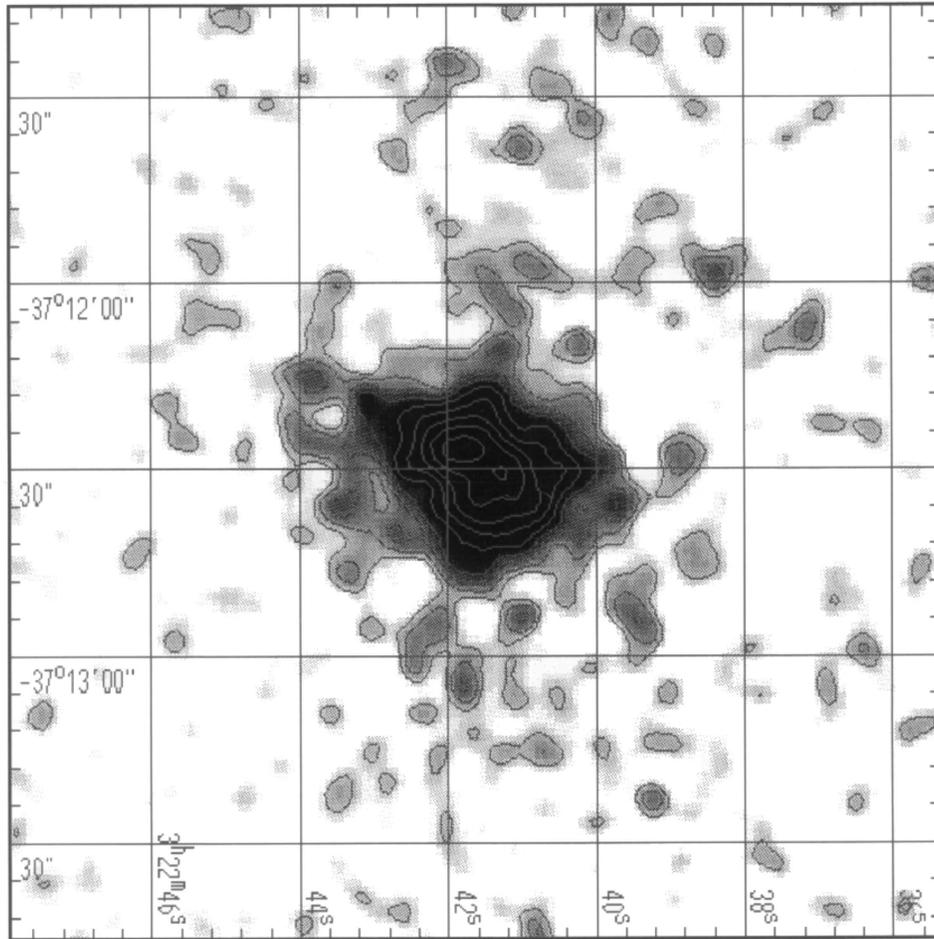
FIG. 4.—Same as Fig. 2, but with a pixel size of 1″ and a Gaussian σ of 2″. Data obtained only in the July run are used. Contours indicate isophotes at 6%–85% of the peak with eight steps.

the radial profile of the X-ray surface brightness. Using the radial profile within $r = 180″$ (to minimize the contribution of extended IC emision; see § 2.3 and Feigelson et al. 1995), and a background count rate estimated at $r = 1800″–2400″$
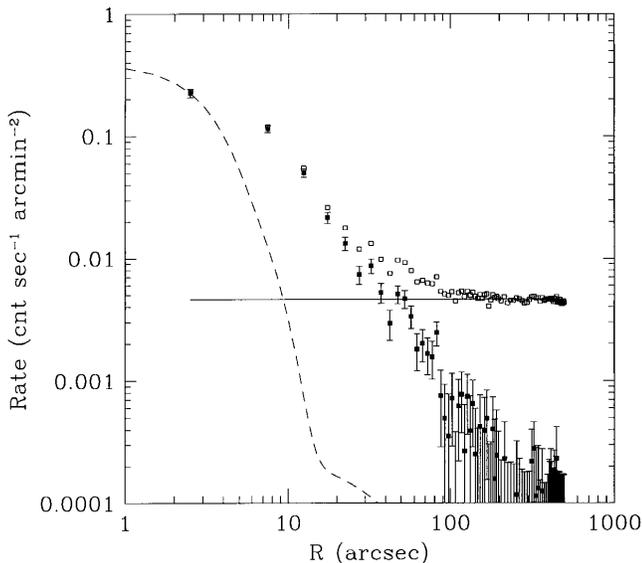

FIG. 5.—Radial distribution of X-ray counts determined with the raw, unsmoothed image. Raw, background (determined at $r = 200″–400″$) and net counts are indicated by open squares, a solid line, and filled squares with error bars.

(with vignetting correction), we find $\Sigma_X \sim r^{-2.25(2.12-2.45)}$, consistent with the HRI profile.

Fits to the radial profiles at the position angles of Figure 3, which take into account the central flattening of the surface brightness give slightly steeper slope [$\beta = 0.56$ (0.52–0.61)] and slightly larger core radius [$a = 6″.2(4.1-8.2)$] along the direction of flattening, whereas the opposite is true along the perpendicular direction [$\beta = 0.46$ (0.43–0.50) and $a = 1″.8(<3.8)$].

A central point source that may be the X-ray counterpart of the radio AGN was not detected with our HRI observations (see the HRI PRF indicated as a dashed line in Fig. 5; see also Fig. 4). To estimate an upper limit to a central point source, we applied the King model plus the HRI point spread function in fitting the radial profile and determined how strong a central source can be added without having χ^2 too large. We derive an upper limit (90%) for the central source of about 5% of the total counts, which corresponds to a flux of 1.0×10^{-13} ergs s^{-1} cm^{-2} in 0.1–2.4 keV and a luminosity of 9×10^{39} ergs s^{-1}. Here we assumed a power law with an energy index $\alpha_E = 0.7$ and line of sight N_H. Of course, a more luminous AGN would be allowed in the presence of large intrinsic N_H.

The spectral analysis of the extended X-ray emission associated with NGC 1316 (§ 2.3) suggests that over 60% of the flux is likely to be of gaseous origin. In the assumption that most of the extended emission is due to a hot ISM, we have derived its three-dimensional density distribution,

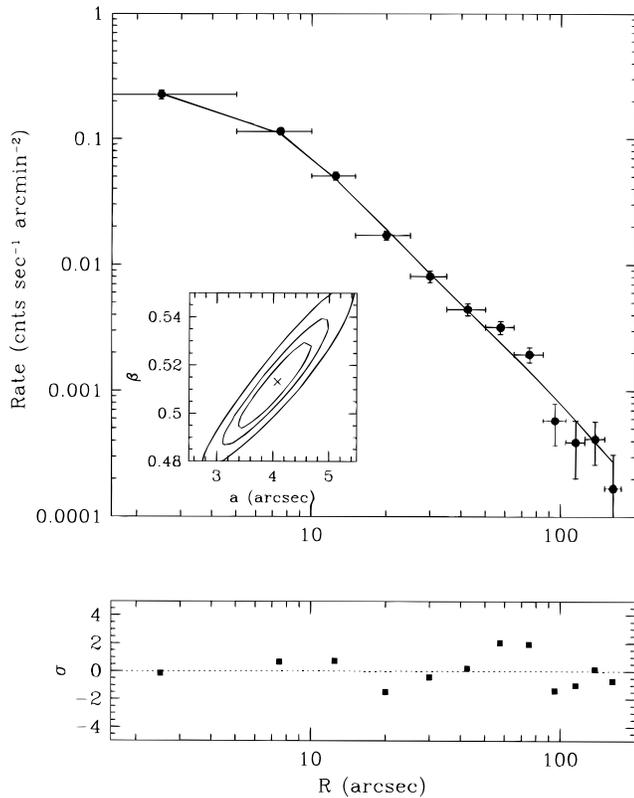*ROSAT* X-RAY OBSERVATIONS OF NGC 1316

FIG. 6.—Radial profile of X-ray surface brightness and best-fit model prediction.

using a direct deprojection method (Kriss, Cioffi, & Canizares 1983), where the emissivity (or density) is inwardly measured by subtracting the contribution of successive spherical layers. We implicitly assume that the hot gas is homogeneous and that the physical status of the gas at a given radius can be represented by one temperature and density. The deprojected density profile is shown in Figure 7a. We have assumed $T = 0.8$ keV (§ 2.3). The density

profile corresponding to $\beta = 0.51$, i.e., $n_e \sim r^{-1.53}$ is also shown as a dashed line in the figure.

Using the deprojected density distribution, we estimate the cooling time and gas pressure as a function of radius (Figure 7b). The cooling time is given as $\tau_c = 1.5[nkT/(n_e n_H \Lambda)]$, where n, n_e, and n_H are the total particle density, electron density, and hydrogen density, respectively, and Λ is the cooling function. The constant is in the range of 1–2.5, depending on its definition (see Sarazin 1988). The cooling time in the center is $\sim 10^8$ yr, much smaller than the Hubble time; it reaches 10^{10} yr at $\sim 180''$. To estimate the cooling function, we assumed solar metal abundances. With the PSPC spectral data (§ 2.3), the metal abundances cannot be determined unambiguously (see also, e.g., Trinchieri et al. 1994; Fabbiano et al. 1994a). The cooling time in the central region is still much shorter than the Hubble time, even, with a zero metal abundance model. We also estimate the thermal gas pressure using the measured density and assuming $kT = 0.8$ keV (Fig. 8).

We point out that these radial dependences of density, cooling time, and pressure are only indicative average values. Because of the complexity of the surface brightness distribution in the inner regions, we would expect a range of these physical parameters at each radius, reflecting the clumpiness of the hot ISM. Also as remarked earlier, we cannot study separately the properties of the different components of the emission suggested by the PSPC data.

2.3. *ROSAT PSPC Spectral Properties*

In order to determine the X-ray spectral properties, we have used the *ROSAT* PSPC data obtained from the public archives. The method of data reduction is similar to that of the PSPC observations of NGC 507 (Kim & Fabbiano 1995). Because the X-ray emission is extended at least out to $1000''$ (see Feigelson et al. 1995 for discussions of the extended structure of X-ray emission), we determined the background at $r = 1800''–2400''$ and applied vignetting correction to each energy channel. Since we are interested in the galaxy emission, we have analyzed the X-ray emission
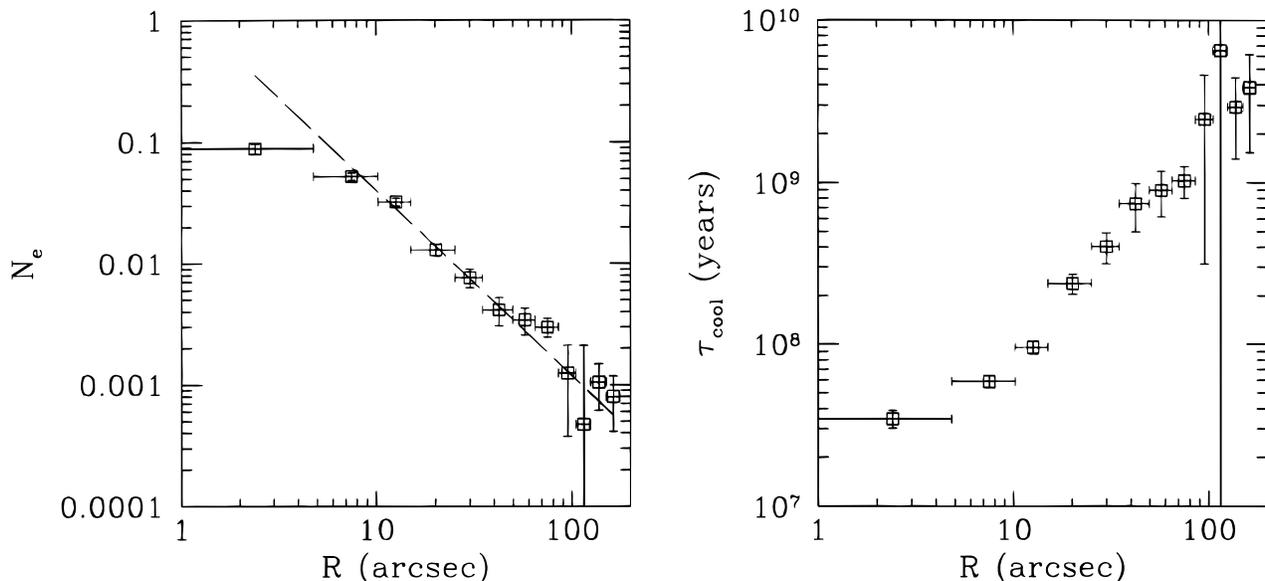

FIG. 7.—(a) Deprojected density and (b) cooling time as a function of radius. The density profile corresponding to $\beta = 0.51$ ($n_e \sim r^{-1.53}$) is shown as a dashed line.
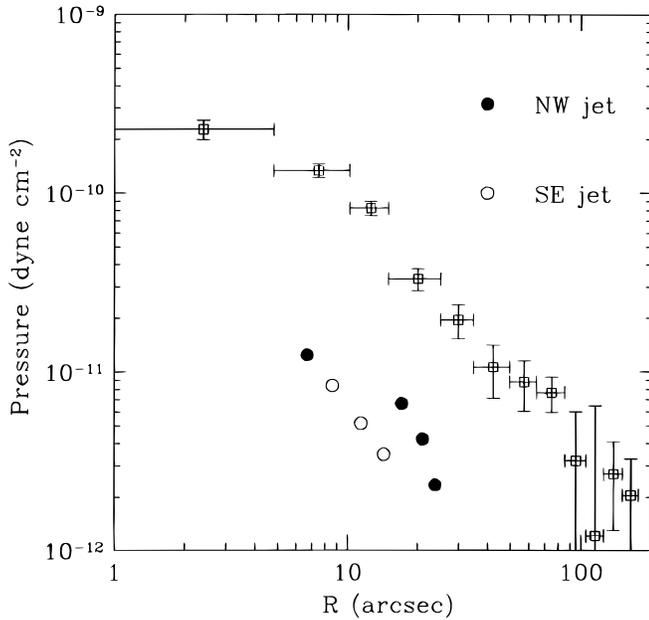
FIG. 8.—Thermal gas pressure as a function of radius. The minimum radio pressure along the jets is also plotted with filled circles (the northwest jet) and open circles (the southeast jet).

within 180″ from the center. Feigelson et al. (1995) found inverse Compton (IC) radiation at the location of the extended radio lobes. The slope of the X-ray radial profile changes abruptly at $r \sim 180″$, indicating that the X-ray emission in the central region has a different origin from that of the extended X-ray emission (Feigelson et al. 1995). To check for possible contribution of IC radiation to the X-ray emission within $r < 180″$, we also estimated the background using portions of the field within the PSPC support structure ($r \sim 1000″$) where the diffuse emission is least. However, the results are not significantly different.

Using XSPEC, we found that the X-ray spectra within 180″ can be well reproduced either by a one-temperature, low-abundance model ($kT \simeq 0.60$–0.7 keV and $\sim 10\%$ solar abundance) or by a two-temperature, low-abundance model ($kT_1 \simeq 0.1$–0.2 keV and $kT_2 \simeq 0.8$–0.9 keV at 90% confidence). In both cases, the acceptable range of N_H is

consistent with the Galactic line-of-sight value (2×10^{20} cm^{-2}). The best-fit parameters and acceptable ranges with N_H fixed at the line-of-sight value are listed in Table 4. Although we prefer the two-component model rather than the almost zero-abundance model (see § 5.1), both models suggest a significant amount of hot gaseous emission because a significantly higher kT would be expected from a population of LMXB (see the analysis of the M31 bulge data by Fabbiano, Trinchieri, & van Speybroeck 1987). We do not see any radial variations in the spectral parameters (temperature and N_H) with the PSPC observations (Table 4).

The absorption-corrected X-ray flux for the best-fit parameters is 2×10^{-12} ergs s^{-1} cm^{-2} (see Table 5), corresponding to a X-ray luminosity of 1.8×10^{41} ergs s^{-1} at the adopted distance of 27.2 Mpc. The HRI flux is consistent with the *Einstein* IPC flux (see Table 1). For the two-component model, the X-ray flux of the very soft component is $\sim 40\%$ of the total flux in 0.1–2.4 keV, similar to those seen in other X-ray–faint early-type galaxies (Fabbiano et al. 1994a; Fabbiano & Schweizer 1995). These results indicate the presence of hot ISM contributing at least 60% of the total X-ray emission even if the soft component is fully of stellar origin.

The analysis of the HRI image (§ 2.2) shows that a nuclear point source cannot contribute significantly to the emission in the *ROSAT* band. Therefore the spectral parameters (even in the outermost bin) are representative of an extended emission component. To estimate the upper limits of hard X-ray emission from low-mass binaries to this emission [as seen in the bulges of spirals (Fabbiano 1989) and in ellipticals (Matsushita et al. 1994; Matsumoto et al. 1997)], we added a hard bremsstrahlung component in the spectral fitting and determined the acceptable range of its normalization. Its temperature was allowed to vary between 3 and 20 keV. The 90% upper limit of the hard component is 15% of the total flux in 0.1–2.4 keV for a one-temperature, low-abundance model and 20% for a two-temperature, solar-abundance model. Even if we restrict our analysis to the central 1′ region, the contribution of the hard component is less than 20% for a one-component model and 30% for a two-component model. This upper limit corresponds to fluxes of 3–4×10^{-13} ergs s^{-1} cm^{-2} and lumi-

TABLE 4

SPECTRAL FIT OF PSPC DATA[a]

TWO-COMPONENT FIT WITH SOLAR ABUNDANCE[b]

Radius (arcsec)	kT_1 (keV)	kT_2 (keV)	Norm[c]	χ^2	Degrees of Freedom
0–60	0.16 (0.13–0.20)	0.83 (0.76–0.90)	1.68 (1.44–1.88)	26.61	23
60–180	0.15 (0.11–0.17)	0.86 (0.72–1.04)	0.74 (0.54–1.03)	17.89	23
0–180	0.16 (0.14–0.17)	0.84 (0.79–0.89)	1.23 (1.08–1.38)	25.34	23

ONE-COMPONENT FIT WITH VARYING ABUNDANCE[d]

Radius (arcsec)	kT (keV)	Abundance (solar)	χ^2	Degrees of Freedom
0–60	0.70 (0.65–0.77)	0.12 (0.10–0.15)	14.36	24
60–180	0.59 (0.48–0.70)	0.03 (0.02–0.05)	21.14	24
0–180	0.68 (0.63–0.73)	0.08 (0.06–0.10)	12.99	24

[a] N_H is fixed at the Galactic line-of-sight value, 2×10^{20} cm^{-2}.
[b] Errors are at 90% confidence, with three interesting parameters.
[c] Normalization of the second component relative to the first component.
[d] Errors are at 90% confidence, with two interesting parameters.

TABLE 5

X-RAY FLUX AND LUMINOSITY[a]

Model	Flux[b]	Luminosity[c]
One-component model:		
Total	$1.9(\pm 0.2) \times 10^{-12}$	$1.7(\pm 0.2) \times 10^{41}$
Upper limit of hard binary component	2.9×10^{-13}	2.6×10^{40}
Upper limit of nuclear component[d]	1.0×10^{-13}	8.9×10^{39}
Two-component model:		
Total	$2.0(\pm 0.2) \times 10^{-12}$	$1.8(\pm 0.2) \times 10^{41}$
0.2 keV component	$8.1(\pm 1.0) \times 10^{-13}$	$7.2(\pm 0.9) \times 10^{40}$
0.8 keV component	$1.2(\pm 0.1) \times 10^{-12}$	$1.1(\pm 0.1) \times 10^{41}$
Upper limit of hard binary component	4.0×10^{-13}	3.6×10^{40}
Upper limit of nuclear component[d]	1.0×10^{-13}	8.9×10^{39}

[a] Data with $r < 180''$ are used, and errors are based on the acceptable range of normalization at 90%.
[b] Absorption-corrected flux in units of ergs s^{-1} cm^{-2} in 0.1–2.4 keV.
[c] Distance = 27.2 Mpc.
[d] Estimated from the HRI image.

nosities of 3–4×10^{40} ergs s^{-1} (Table 5). The X-ray to optical luminosity ratio is then $L_X/L_B \leq 2$–3×10^{29} ergs s^{-1} $L_\odot^{-1}$ and is consistent with that of the bulge of M31 where the X-ray emission is dominated by a population of individual bright X-ray sources (see, e.g., Trinchieri & Fabbiano 1991) and with those of hard components in other early-type galaxies observed with *ASCA* (Matsumoto et al. 1997).

3. COMPARISON WITH OTHER WAVELENGTH DATA

Figures 9, 10, and 11 compare the high-resolution HRI contour map of Figure 2 with the distribution of dust (Schweizer 1980), ionized gas, and radio continuum (Geldzahler & Fomalont 1984), respectively. Although the low signal-to-noise ratio nature of the X-ray data is such that a definitive, quantitative comparison cannot be done,
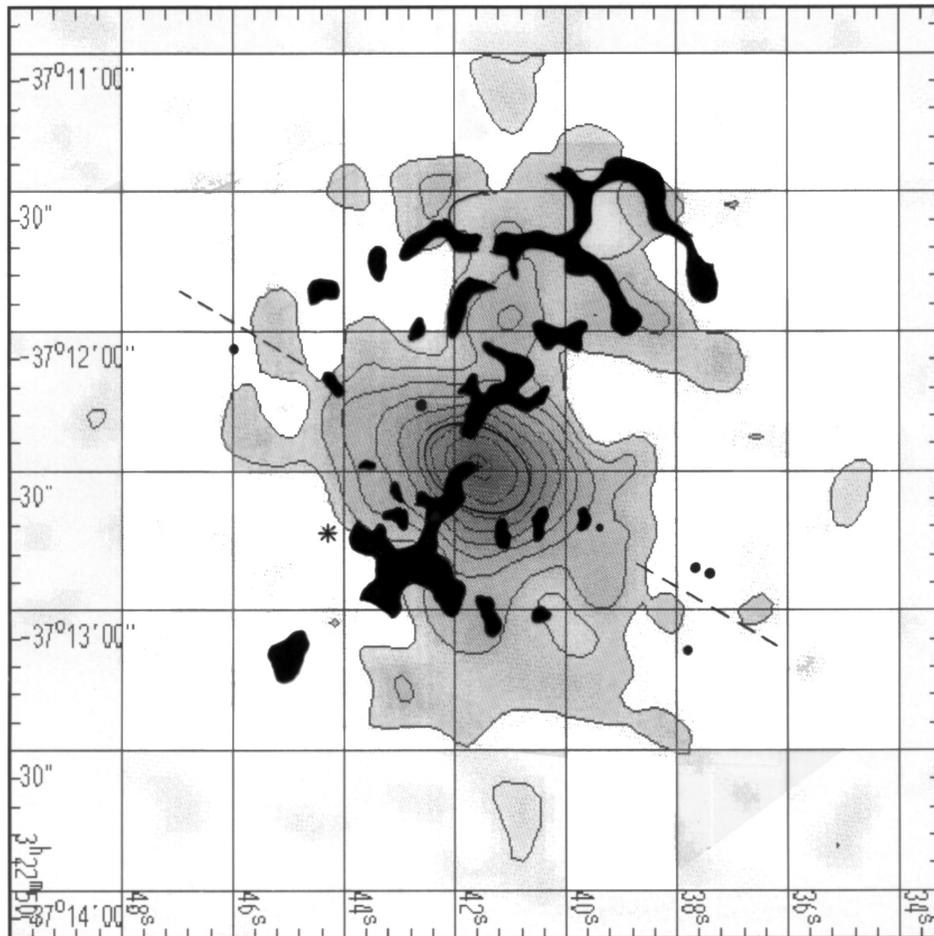

FIG. 9.—Distribution of dust patches from Schweizer (1980) overlaid onto the X-ray image (same as Fig. 2)
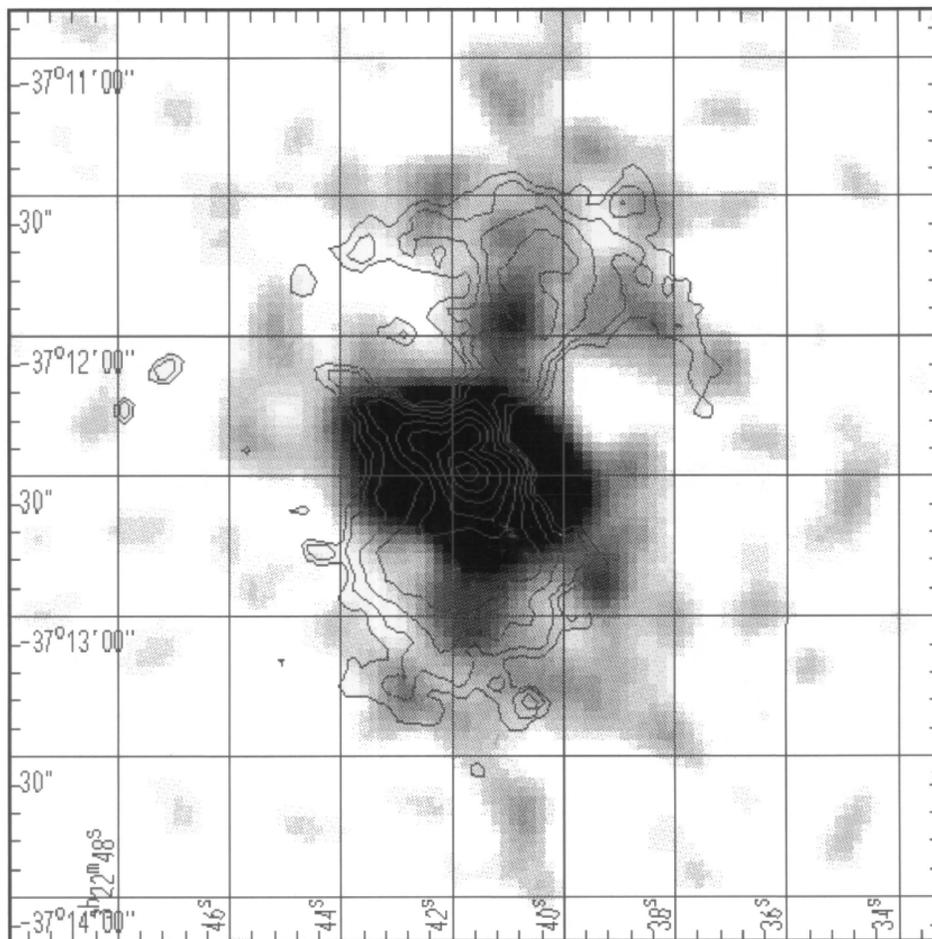
FIG. 10.—Distribution of ionized gas overlaid onto the X-ray image. Continuum-subtracted Hα + [N II] image was smoothed with a 2 pixel (full width) Gaussian filter; X-ray image is the same as Fig. 2.

there are some qualitative trends that it is worth to mention.

In general, the hot and cold ISM are related in the sense that the X-ray emission is significantly reduced at the locations where the dust patches are most pronounced. In particular, a dust lane is found in the central southeast X-ray valley, suggesting the possibility of absorption.

Because the ionized gas may be originated from the cooling hot gas, the distribution of ionized gas provides further clues of the relationship between cold and hot ISM. Narrowband CCD images were taken on the photometric night of 1994 November 11–12. The CTIO/University of Michigan Curtis Schmidt 0.6/0.9 m telescope was used with a Thomson 1024×1024 CCD. Pixel size is 19 μm square (1″.835); however, vignetting limits the usable field size to about 30′. Total exposure times were 8100 s each for the redshifted ($v = 1801$ km s^{-1}) Hα + [N II] ($\lambda6563 + \lambda\lambda6548$, 6583) emission-line filter ($\lambda_c = 6606$ Å, FWHM = 76 Å), and continuum filter ($\lambda_c = 6693$ Å, FWHM = 81 Å). Bias and dark frames were taken. Flat fields were generated from twilight sky exposures. The spectrophotometric standard HZ 4 was used to calibrate the narrow-band images on AB magnitudes (J. B. Oke 1994, private communication). The adopted magnitudes were $AB_{6606} = 15.01$ and $AB_{6693} = 14.81$. The Hα + [N II] image was derived by subtracting a scaled, sky-subtracted continuum image from the sky-subtracted emission-line image. The adopted scaling was calculated from a linear least-squares fit to residuals of 25

field stars calculated from several scaling factors. The mean pixel value of the Hα + [N II] image at large radii of the optical galaxy was also consistently near zero. The distribution of ionized gas is shown in Figure 10, superposed on the X-ray image (same as Figure 2). The overall distribution of the ionized gas is similar to that of the dust, i.e., aligned toward north-south, slightly turned to northwest and southeast (clockwise), as observed in other early-type galaxies with cold ISM (Kim 1989). The peak of the northern blob (40^s.5, 11″.8) falls in between the dust patches, likely due to dust absorption. The eastern part of the southern blob generally follows the distribution of the dust patch. Comparing the distributions of hot and warm ISM, we also find an overall similarity (e.g., north-south extension), but there is not always a one-to-one correspondence.

Figure 11a shows the radio jets superposed on the X-ray image (same as Fig. 2). This radio image was reproduced from Figure 2b in Geldzahler & Fomalont (1984), which was obtained with the VLA and has 4″ resolution at 1.5 GHz. The direction of the radio jet is in projection perpendicular to the direction of northeast-southwest elongation of the central X-ray distribution. If confirmed, the X-ray valleys (seen in Fig. 4) may imply even more striking relations in that both sides of the radio jets in projection coincide with the X-ray valleys at P.A. $\simeq 120°$ and P.A. $\simeq 320°$ (Fig. 11b), suggesting that the radio jets are interacting with the surrounding hot gaseous medium as seen in Cygnus A (Carilli, Perley, & Harris 1994).
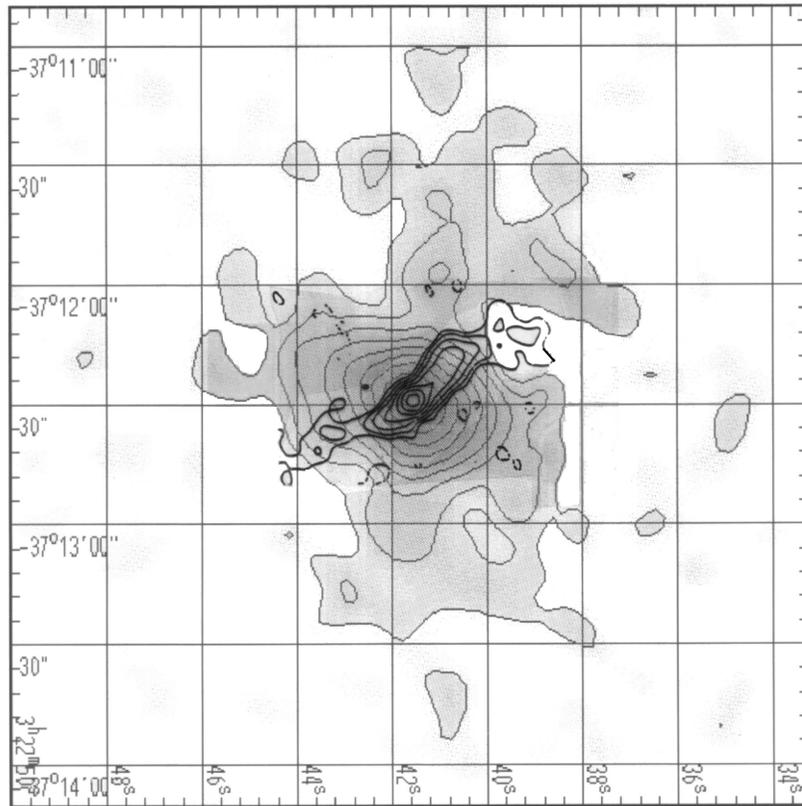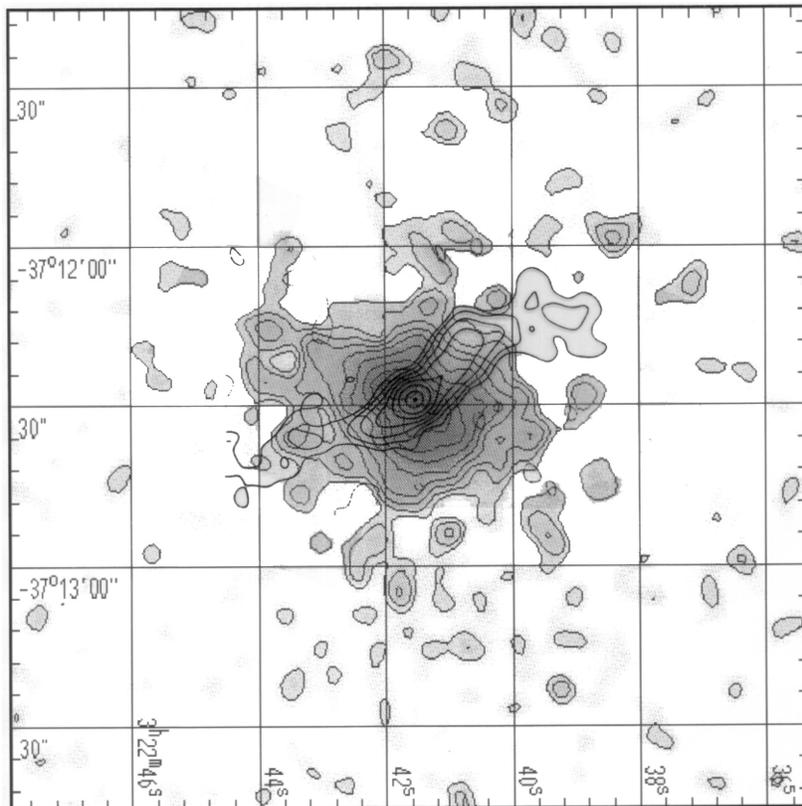
Fig. 11a

Fig. 11b

Fig. 11.—Radio jet overlaid onto the X-ray image. Radio map was taken from Geldzahler & Fomalont (1984). X-ray image is the same as (a) Fig. 2 and (b) Fig. 4.

These connections need to be checked with future high-resolution observations. The AXAF CCD detector will provide 1″ resolution data with spectral resolution as well, which will be ideally suited for this type of investigation.

4. DISCUSSION

4.1. *The Nature of X-Ray Emission of NGC 1316*

The X-ray emission of E and S0 galaxies can be due to different sources (see Fabbiano 1989): a hot gaseous halo dominating the emission in the X-ray–bright early-type galaxies; integrated stellar X-ray binary emission, seen in the bulges of spirals (see Fabbiano 1989) and confirmed in ellipticals with *ASCA* (Matsushita et al. 1994; Matsumoto et al. 1997); a nuclear source, seen in bright radio galaxies (Fabbiano et al. 1984; Worrall & Birkinshaw 1994); and a very soft component, seen in X-ray–faint early-type galaxies (Kim et al. 1992b; Fabbiano et al. 1994a; Kim et al. 1996) of debatable nature (e.g., Pellegrini & Fabbiano 1994). NGC 1316 is both an X-ray–faint D (maybe cD) galaxy and a radio galaxy; therefore, its X-ray emission is likely to be complex.

With the HRI imaging data and the PSPC spectral data, we can limit the contribution from the nuclear component and stellar binary component, respectively, as being relatively unimportant to the detected X-ray emission (Table 5). The upper limit to the nuclear X-ray emission obtained with the HRI image (§ 2.2) is $L_X \leq 9 \times 10^{39}$ ergs s^{-1}, which is about 5% of the total luminosity. Of course, a more luminous nuclear source could be present and not visible if the nuclear N_H is much higher than the line-of-sight one. With the PSPC spectra, we can pose a upper limit to the hard stellar component of 20%–30% of the total flux in 0.1–2.4 keV ($L_X \leq 3$–4×10^{40} ergs s^{-1}; § 2.3). This is consistent with the expected hard X-ray emission from a "bulge" population of X-ray sources (e.g., scaling from the M31 bulge; Trinchieri & Fabbiano 1991). Individual typical X-ray binary sources would not be detectable at the luminosity threshold of our observation (a few × 10^{39} ergs s^{-1}).

The PSPC spectrum of NGC 1316 (§ 2.3) suggests that most of the X-ray emission within 3′ is due to a hot ISM in this galaxy. Although with the PSPC data we cannot unequivocally define the emission model, the spectral fits require the presence of a ∼0.7–0.9 keV thermal emission (Table 4). The X-ray spectrum of NGC 1316 resembles that of other X-ray–faint early-type galaxies. X-ray spectra of those galaxies observed both with the IPC (Kim et al. 1992a) and the PSPC (see, e.g., Fabbiano et al. 1994a) present an excess of counts in the lowest energy channels, when compared to those of X-ray–bright E and S0 galaxies. This type of spectrum can be fitted either with a metal-free single-temperature optically thin model or with two (or more) component models (see Fabbiano et al. 1994a; Pellegrini & Fabbiano 1994; Fabbiano & Schweizer 1995). Recent *ASCA* measurements of the spectrum of the X-ray–faint galaxy NGC 4382 (Kim et al. 1996) reject the single-component metal-free model in that galaxy. The two-component model, in the case of NGC 1316, would consist of a very soft component of $kT \sim 0.1$–0.2 keV (which could be of stellar origin; see, e.g., Pellegrini & Fabbiano 1994), and a harder ($kT \sim 0.7$–1.0 keV), almost solar metallicity ISM. It is interesting that the abundance of the ISM determined from this two-component model is near to the optical metallicity of this galaxy (see, e.g., Gorgas, Efsta-

thiou, & Salamanca 1990). However, based on more general *ASCA* results on galaxies (see, e.g., Loewenstein et al. 1994; Arimoto et al. 1997), the latter may just be a coincidence.

Although a hot ISM is present, the total amount of hot gas is ∼10^9 $M_\odot$, only a fraction of that present in X-ray–bright early-type galaxies with a comparable optical luminosity (for example, $M_{gas} \sim 2 \times 10^{10}$ $M_\odot$ in NGC 4636; Trinchieri et al. 1994). NGC 1316 clearly has not been accumulating all the gas ejected from the evolved stars during a Hubble time, which would be ∼3 × 10^{10} $M_\odot$. This is not surprising since this galaxy may have undergone recent merging events (see Schweizer 1980). Recent mergers (Hibbard et al. 1994) and dynamically young ellipticals (Fabbiano & Schweizer 1995) also tend to be relatively empty of hot ISM. It may be a coincidence, but the mass of the hot ISM is comparable with what would be expected from stellar accumulation in ∼1 Gyr, which may be the age of merger (Schweizer 1980). In a recent paper discussing the optical and X-ray emission at larger radii, Mackie & Fabbiano (1998) find ∼3 × 10^8 $M_\odot$ of hot ISM spatially coincident with the tidal tails in the outskirts of NGC 1316.

4.2. *Multiphase ISM*

The comparison between X-ray and optical data reveals that the distribution of the X-ray emission is related with that of dust patches (§ 3.1). The X-ray emission is weak where dust is seen, and X-ray blobs are often surrounded by dust patches. The X-ray valleys running toward northwest and southeast from the center (Fig. 4), if confirmed, may be real low-density regions in the hot ISM because they are not coincident with dust patches, except in the central southeast region. The ionized gas is overall cospatial with the dust patches. However, the northern blob of the ionized gas falls in between dust patches, while the southern blob coexists with dust, indicating some of the line emission is absorbed by the dust.

The origin of the ionized gas (i.e., ionization mechanism) is unclear in early-type galaxies. The emission lines often indicate LINER-type nuclear activity rather than H II regions, judged by, for example, the relative line strengths Hα to [N II] flux ratio (see, e.g., Kim 1989). It has also been suggested that the gas is photoionized by post-AGB stars (Trinchieri & di Serego Alighieri 1991). In the case of galaxies containing significant amounts of hot ISM, the ionized gas may also be the result of cooling flows (see, e.g., Sarazin 1988), but this is unlikely in NGC 1316.

In NGC 1316, the kinematics of the ionized gas revealed that the gas is rapidly (up to 350 km s^{-1}) rotating along the major axis (P.A. = 127°–142°; Schweizer 1980), while the stellar system rotates along the major axis (P.A. = 50°; Bosma, Smith & Wellington 1985). The same is true for molecular gas (Sage & Galletta 1993). This suggests an external origin for the cold and ionized ISM, perhaps connected with the merging episode (Schweizer 1980; Mackie & Fabbiano 1997) and argues against the idea that the ionized/cold gas is originated from cooling hot gas. In the latter case both hot and cold/warm gas would be expected to have the same kinematics as the star since the hot ISM is likely to originate from stellar evolution. Different origins of warm gas (likely cold gas and dust as well) and hot gas may be further supported by our HRI observations in that the central X-ray flattening, possibly a disk would rotate along the major axis and that the morphological relationships between the ionized gas and the X-ray emission are lacking.

Therefore, it is likely that the cold and warm ISM might be acquired externally by mergers and infalls occurring $\sim 10^9$ yr ago, while the hot gas has been accumulated since the latest merger.

If the infalling, cooling hot ISM carries angular momentum, it may form an accretion disk, which could extend out to a 10 kpc radius (see Kley & Mathews 1995; Brighenti & Mathews 1996). The northeast-southwest flattened isophotes of NGC 1316 (Fig. 2) may represent such a disk. However, because the isophotes are measured at radii less than the optical effective radius, the stellar potential needs not be round at these radii. Therefore, the observed elongation may be consistent with hydrostatic gas in the stellar potential (or with a modest amount of dark matter).

4.3. *Is the Radio Jet Thermally Confined?*

Interestingly, the observed elongation in the hot gas structure is approximately perpendicular to the radio jet of NGC 1316. The possibility of thermal confinement is supported by the radial behavior of the jet/ISM energetics. We estimated the radio jet pressure corresponding to the minimum energy using the radio map by Geldzahler & Fomalont (1984) (see Feigelson et al. 1995 for the validity of the minimum energy argument). We applied the prescription for a Gaussian jet given in Kileen, Bicknell, & Ekers (1986a; see also Pacholczyk 1970). We also used the cylindrical jet approximation (see Perley, Willis, & Scott 1979), but the results do not change significantly. We assumed that the jet and the magnetic field are perpendicular to the line of sight; that the energy of relativistic electrons is equal to that of protons and ions; that the radio spectrum is a power law from 10 MHz to 10 GHz with a slope $\alpha = 0.7$; and that the volume filling factor is unity. The estimated jet pressure is compared with the thermal pressure in Figure 8. At 6″–24″ from the center, the jet pressure for both northwest and southeast jets is one order of magnitude lower than the thermal pressure. Radio and thermal pressure are supposed to be in the balance in the case of thermal confinement. However, as discussed by Killeen, Bicknell, & Ekers (1988) the radio minimum pressure could be easily underestimated (see also Pacholczyk 1970), while the similarity of the radial behavior of radio and X-ray pressures argues for thermal confinement. This apparent contradiction between the thermal gas and minimum radio pressures has also been reported in similar cases where radio jets are expanding through the hot gaseous environment (see, e.g., Bohringer et al. 1993; Carilli et al. 1994).

The possibility (suggested by Fig. 8) that the jet is thermally confined inside a relatively small region reinforces the suggested lack of causal connection between the jet and the extended lobes (Ekers et al. 1983). It is possible that active events took place some time ago, probably induced by a merger ($\sim 10^9$ yr ago; Schwiezer 1980), and now the nucleus is relatively weak and the radio lobes are slowly cooling (see also Ekers et al. 1983). This idea is also supported by the relative power ($\sim 1/2500$) of the jets to the extended radio lobes, which is a few hundred times lower than that of a typical early-type galaxy (Slee et al. 1994), the lack of strong optical emission lines (see Schweizer 1980), the absence of a connection between the jet and the lobe (Geldzahler & Fomalont 1984), and the morphology of the lobes (Fomalont et al. 1989).

The double peaks and X-ray valleys seen in Figure 4, if confirmed, will provide more direct evidence for interaction

betweeen the hot gas and the radio jet. Both sides of the radio jets in projection appear to pass through the X-ray valleys which may play a role as nozzles in collimating the jets.

4.4. *The Nucleus*

Fabbiano et al. (1984) found a relationship between radio core power and X-ray luminosity in a sample of 3 CR galaxies, indicating that both radio and X-ray emission are of nonthermal nuclear origin. This relationship holds down to radio-faint galaxies (Fabbiano, Gioia, & Trinchieri 1989). Recently, with *ROSAT* observations, Worrall & Birkinshaw (1994) spatially decomposed central X-ray point sources from the diffuse, extended emission in several radio galaxies and confirmed the linear relationship between core radio and central X-ray emission in low-power radio galaxies. Although the X-ray core of NGC 1316 is not detected, the ratio between the X-ray upper limit (corresponding to $l_{1\,\mathrm{keV}} \leq 6.3 \times 10^{21}$ ergs s^{-1} Hz^{-1}) and the radio core emission ($l_{5\,\mathrm{GHz}} = 2 \times 10^{28}$ ergs s^{-1} Hz^{-1}, from Geldzahler & Fomalont 1984) is consistent with the linear relationship between these quantities discussed above.

A comparison of the spectral energy distribution (SED) of the NGC 1316 nucleus with those of other LINER galaxies can be found in Fabbiano & Juda (1998). It is worth noting the possible similarity between the nuclear sources of NGC 3998 and NGC 1316 (both early-type galaxies). They both present a bright UV pointlike source discovered with *HST*, and their SEDs differ from those of bright AGNs (see also Fabbiano et al. 1994b). A better coverage of the nuclear emission of these faint AGNs will be necessary to understand the emission mechanism.

5. CONCLUSION

We have presented the analysis of the high spatial resolution image and of the X-ray spectrum of NGC 1316 (Fornax A) obtained with the *ROSAT* HRI and PSPC. The results lead to the following conclusions:

1. The X-ray emission of NGC 1316 is extended. No point sources are detected within the galaxy at a luminosity threshold of a few $\times 10^{39}$ ergs s^{-1}. The radial profile of the X-ray surface brightness falls as r^{-2}, which is close to the optical light distribution. No gradient of the X-ray emission temperature is seen. Within the central 40″, the X-ray isophotes are flattened along the optical major axis. In a larger scale (1′–2′), the X-ray emission is extended toward north-south, in agreement with the PSPC report of inverse Compton emission (Feigelson et al. 1995).

2. The X-ray spectrum of NGC 1316 ($r < 180″$) can be reproduced either by a single-temperature low-abundance model ($kT = 0.7$ keV and 10% solar) or by a two-temperature solar-abundance model ($kT_1 = 0.1$–0.2 keV and $kT_2 = 0.8$–0.9 keV). These results indicate the presence of hot gaseous component contributing to greater than 60% of the total X-ray emission. We set an upper limit of $\sim 20\%$ of the total emission due to a hard component from LMXB in NGC 1316, consistent with an extrapolation based on the bulge of M31 as well as those of early-type galaxies observed with *ASCA*. The total X-ray emission is 2×10^{41} ergs s^{-1} in the 0.1–2.4 keV band and $M_{\mathrm{gas}} \sim 10^9\ M_\odot$. The relatively small amount of hot ISM present in this X-ray–faint galaxy (by comparison with that of X-ray–bright E and S0 galaxies such as NGC 4636 and NGC 4472; see, e.g.,

Fabbiano et al. 1992) is consistent with observations of other systems that may have undergone relatively recent merging (Fabbiano & Schweizer 1995).

3. The X-ray emission is significantly reduced at the locations where the dust patches are more pronounced, indicating that some of the X-ray emission may be absorbed by the internal cold ISM in NGC 1316. The ionized gas is generally distributed along with the dust patches. Some features of the ionized gas appear to be related with a hot ISM but there is no one-to-one correspondence. Both morphological relations and kinematics suggest that the hot and cold/warm ISM may not have the same origin. The cold/warm ISM might be acquired externally by mergers/infalls, while the hot ISM has been accumulated since the latest merger.

4. In projection, the direction of the radio jets is perpendicular to the central northwest-southeast elongation of the X-ray emission. The thermal pressure is higher than the jet equipartition pressure by one order of magnitude. However, the radial behavior of thermal and radio pressures are similar, suggesting the possibility of thermal confinement.

5. Although a nuclear source is not detected in X-rays, the upper limit ($L_X \leq 9 \times 10^{39}$ ergs s^{-1}) is consistent with the expectations, based on the extrapolation from low-power radio galaxies (Worrall & Birkinshaw 1994).

REFERENCES

Arimoto, N., Matsuchita, K., Ishimaru, Y., Ohashi, T., & Renzini, A. 1997, ApJ, 477, 128
Arp, H. 1966, ApJS, 14, 1
Baum, S. A., Heckman, T. M., & van Breugel, W. 1992, ApJ, 389, 208
Bohringer, H., Voges, W., Fabian, A. C., Edge, A. C., & Neumann, D. M. 1993, MNRAS, 264, L25
Bosma, A., Smith, R. M., & Wellington, K. J. 1985, MNRAS, 212, 301
Brighenti, F., & Mathews, W. 1996, ApJ, 470, 747
Buote, D. A., & Canizares, C. R. 1994, ApJ, 427, 86
Carilli, C. L., Perley, R. A., & Harris, D. E. 1994, MNRAS, 270, 173
Carter, D., Jorden, P. R., Thorne, D. J., Wall, J. V., & Straede, J. C. 1983, MNRAS, 205, 377
Carter, D., & Metcalfe, N. 1980, MNRAS, 191, 325
David, L. P., Harnden, F. R., Kearns, K. E., & Zombeck, M. V. 1993, The *ROSAT* High Resolution Imager, US *ROSAT* Science Data Center, SAO
de Vaucouleurs, G., de Vaucouleurs, H., Corwin, H. G., Buta, R. J., Paturel, G., & Fouque, P. 1991 Third Reference Catalogue of Bright Galaxies (New York: Springer) (RC3)
Ekers, R. D., Gross, W. M., Wellington, K. J., Bosma, A., Smith, R. M., & Schweizer, F. 1983, A&A, 127, 361
Fabbiano, G. 1989, ARA&A, 27, 87
Fabbiano, G., Fassnacht, C., & Trinchieri, G. 1994b, ApJ, 434, 67
Fabbiano, G., Gioia, I. M., & Trinchieri, G. 1988, ApJ, 324, 749
———. 1989, ApJ, 347, 127
Fabbiano, G., & Juda, G. 1998, in preparation
Fabbiano, G., Kim, D.-W., & Trinchieri, G. 1992, ApJS, 80, 531
———. 1994a, ApJ, 429, 94
Fabbiano, G., Miller, L., Trinchieri, G., Longair, M., & Elvis, M. 1984, ApJ, 277, 115
Fabbiano, G., & Schweizer, F. 1995, ApJ, 447, 572
Fabbiano, G., Trinchieri, G., & van Speybroeck, L. 1987, ApJ, 316, 127
Feigelson, E. D., Laurent-Muehleisen, S. A., Kollgaard, R. I., & Fomalont, E. B. 1995, ApJ, 449, L149
Fomalont, E. B., Ebnerter, K. A., van Breugel, J. M., & Ekers, R. D. 1989, ApJ, 346, L17
Geldzahler, B. J., & Fomalont, E. B. 1984, AJ, 89, 1650
Gorgas, J., Efstathiou, G., & Aragon Salamanca, A. 1990, MNRAS, 245, 217
Hasinger, G., Burg, R., Giacconi, R., Hartner, G., Schmidt, M., Trumper, J., & Zamorani, G. 1993, A&A, 275, 1
Hibbard, J. E., Guhathakurta, P., van Gorkom, J. H., & Schweizer, F. 1994, AJ, 107, 67
Jedrzejewski, R. I. 1987, MNRAS, 226, 747

Kaneda, H., et al. 1995, ApJ, 453, L13
Kileen, N. E. B., Bicknell, G. V., & Carter, D. 1986b, ApJ, 309, 45
Killeen, N. E. B., Bicknell, G. V., & Ekers, R. D. 1986a, ApJ, 302, 306
———. 1988, ApJ, 325, 180
Kim, D.-W. 1989, ApJ, 346, 653
Kim, D.-W., & Fabbiano, G. 1995, ApJ, 441, 182
Kim, D.-W., Fabbiano, G., & Trinchieri, G. 1992a, ApJS, 80, 645
———. 1992b, ApJ, 393, 134
Kim, D.-W., Fabbiano, G., Matsumoto, H., Koyama, K., & Trinchieri, G. 1996, ApJ, 468, 175
Kley, W., & Mathews, W. 1995, ApJ, 438, 100
Knapp, G. R., Guhathakurta, P., Kim, D.-W., & Jura, M. 1989, ApJS, 70, 329
Kriss, G. A., Cioffi, D. F., & Canizares, C. R. 1983, ApJ, 272, 439
Loewenstein, M., Mushotzky, R. F., Tamura, T., Ikebe, Y., Makishima, K., Matsushita, K., Awaki, H., & Serlemitsos, P. J. 1994, ApJ, 436, L75
Mackie, G., & Fabbiano, G. 1998, ApJ, in press
Malin, D. F., & Carter, D. 1983, ApJ, 274, 534
Matsushita, K., et al. 1994, ApJ, 436, L41
Matsumoto, H., Koyama, K., Awaki, H., Tsuru, T., Loewenstein, M., & Matsushita, K. 1997, ApJ, 482, 133
Pacholczyk, A. G. 1970, Radio Astrophysics (San Francisco: Freeman)
Pellegrini, S., & Fabbiano, G. 1994, ApJ, 429, 105
Perley, R. A., Willis, A. G., & Scott, J. S. 1979, Nature, 281, 437
Phillips, M. M., Jenkins, C. R., Dopita, M. A., Sadler, E. M., & Binette, L. 1986, AJ, 91, 1062
Sage, L. J., & Galletta, G. 1993, ApJ, 419, 544
Sarazin, C. L. 1988, X-ray Emissions from Clusters of Galaxies (Cambridge: Cambridge Univ. Press)
Schweizer, F. 1980, ApJ, 237, 303
———. 1981, ApJ, 246, 722
Slee, O. B., Sadler, E. M., Reynolds, J. E., & Ekers, R. D. 1994, MNRAS, 269, 928
Stark, A. A., Gammie, C. H., Wilson, R. W., Bally, J., Linke, R. A., Heiles, C., & Hurwitz, M. 1992, ApJS, 79, 77
Truemper, J. 1983, Adv. Space Res., 2, No. 4, 241
Trinchieri, G., & di Serego Alighieri, S. 1991, AJ, 101, 1647
Trinchieri, G., & Fabbiano, G. 1991, ApJ, 382, 82
Trinchieri, G., Kim, D.-W., Fabbiano, G., & Canizares, C. R. 1994, ApJ, 428, 555
Véron-Cetty, M. P., & Véron, P. 1986, A&AS, 66, 335
Wade, C. M. 1961, Publ. NRAO, 1, 99
Wiklind, T., & Henkel, C. 1989, A&A, 225, 1
Worrall, D. M., & Birkinshaw, M. 1994, ApJ, 427, 134